Journal of Materials Science and Chemical Engineering, 2025, 13(10), 1-18
https://www.scirp.org/journal/msce
ISSN Online: 2327-6053
ISSN Print: 2327-6045

Optimizing a CIGS Thin-Film Solar Cell with SILVACO ATLAS: Effects of Optical Bandgap and Absorber Electron Affinity

Alioune Ngom[1], Youssou Gning[1], Mamadou Lamine Samb[1*], Aly Toure[1], Moussa Toure[1], Ahmed Mohamed-Yahya[2]

[1]Department of Physics and Chemistry, University Iba Der Thiam of Thies, Thies, Senegal
[2]Applied Research Unit for Renewable Energies, University of Nouakchott, Nouakchott, Mauritania
Email: alioune.ngom2@univ-thies.sn, youssou.gning@univ-thies.sn, *mlsamb@univ-thies.sn, aly.toure1@univ-thies.sn, moussa.toure@univ-thies.sn, biyah2001@yahoo.fr

How to cite this paper: Ngom, A., Gning, Y., Samb, M.L., Toure, A., Toure, M. and Mohamed-Yahya, A. (2025) Optimizing a CIGS Thin-Film Solar Cell with SILVACO ATLAS: Effects of Optical Bandgap and Absorber Electron Affinity. *Journal of Materials Science and Chemical Engineering*, **13**, 1-18.
https://doi.org/10.4236/msce.2025.1310001

Received: September 1, 2025
Accepted: October 13, 2025
Published: October 16, 2025

Abstract

This study uses TCAD numerical simulation to evaluate how key absorber parameters in Cu(In, Ga)Se_2 (CIGS) thin-film solar cells influence device performance, with the objective of identifying low-material, cost-effective optimization strategies. While crystalline-silicon (c-Si) still dominates the market despite its indirect bandgap and the thick wafers it requires, the CIGS pathway, featuring a direct, composition-tunable bandgap and a high absorption coefficient, on glass or flexible polymer substrates, offers a compelling alternative. The device investigated adopts the stack Al/ZnO/CdS/CIGS/Mo/PET and is simulated in SILVACO ATLAS (drift-diffusion transport coupled to Poisson and carrier-continuity equations) under conditions close to STC (AM1.5G, 27˚C, 1000 W·m^{-2}). Parameter sweeps cover the absorber optical bandgap $g \in [1.14, 1.50]$ eV, electron affinity $\chi \in [4.0, 4.8]$ eV, and CIGS thickness $d \in [0.1, 3.0]$ μm, with p-type doping fixed at 1×10^{16} cm^{-3}. The results show that the short-circuit current density J_{sc} is nearly invariant with respect to E_g and χ once the absorber is sufficiently thick ($d \geq 0.3$ μm); a deviation appears at $d = 0.1$ μm , attributed to stronger optical losses (residual transmission) and less efficient carrier collection. In contrast, the open-circuit voltage V_{oc} increases markedly with E_g over the investigated range (consistent with a reduced effective saturation current), which in turn raises the fill factor FF and the power-conversion efficiency η. The electron affinity χ has little influence on J_{sc} (except for $d < 0.3$ μm), but it systematically impacts V_{oc} , FF , and η\eta$\eta$ via band alignment at the buffer/absorber interface. Within our parameter window, a maximum efficiency of about

27.05% is achieved for $E_g \approx 1.50$ eV with $d = 3.0$ μm, where gains in V_{oc} and FF compensate the near-invariance of J_{sc}. Moreover, electron-affinity windows of $\chi \approx 4.0$ - 4.2 eV and $\chi \approx 4.6$ - 4.8 eV are shown to be favorable across 0.1 - 3.0 μm. These findings suggest that joint engineering of composition (Ga content) to tailor E_g and of band alignment (through χ and the CdS/CIGS/ZnO interfaces) is a robust route to boost CIGS efficiency while minimizing material usage.

Keywords

CIGS Thin-Film Solar Cells, Optical Bandgap, Electron Affinity, Band Alignment (CdS/CIGS), Open-Circuit Voltage, Fill Factor, Power-Conversion Efficiency

1. Introduction

The global photovoltaic market remains largely dominated by crystalline-silicon (c-Si) solar cells, a mature, industrialized technology known for reliability, high field efficiencies, and long service lifetimes. Silicon is abundant, low-toxicity, and low-cost, and it can be readily doped with boron or phosphorus. Nevertheless, intrinsic limitations, an indirect bandgap ($E_g \approx 1.12$ eV) and a low absorption coefficient (~104 cm^{-1}), necessitate thick wafers (≥100 μm) to efficiently absorb the solar spectrum, which raises material and energy consumption and, ultimately, costs [1].

These constraints have fueled growing interest in thin-film technologies, which aim to reduce material usage and manufacturing costs while maintaining competitive performance [2]. Among them, Cu(In, Ga)Se_2 (CIGS) stands out for its high absorption coefficient and direct, composition-tunable bandgap (≈1.04 - 1.68 eV with gallium content), as well as its compatibility with diverse substrates (glass, flexible polymers) and multiple deposition routes (co-evaporation, sputtering, PLD, screen printing), enabling flexible and Cd-free architectures [2]-[6]. These attributes motivate the performance optimization of CIGS thin-film devices, the focus of the present study.

The objective here is to quantify the influence of two key absorber parameters, the optical bandgap E_g and the electron affinity χ, on the main figures of merit: short-circuit current density J_{sc}, open-circuit voltage V_{oc}, fill factor FF, and power-conversion efficiency η. To this end, we numerically simulate a laboratory-grade CIGS device using TCAD SILVACO-ATLAS, solving Poisson and carrier-continuity equations coupled through the drift-diffusion transport model [3] [7] [8].

The paper is organized as follows. Section 2 revisits the electrical modeling and the characteristic parameters of CIGS cells (equivalent circuit, $J(V)$ relation, J_{sc}, V_{oc}, FF, and η). Section 3 details the materials, device structure, method,

and simulation settings. Section 4 presents the results, followed by their analysis and discussion.

2. Modeling and Electrical Parameters of CIGS Thin-Film Solar Cells

2.1. Equivalent Electrical Circuit

A CIGS solar cell is a p-n heterojunction (p-type CIGS absorber, n-type buffer layer, and TCO window). Its electrical behavior is classically modeled by a two-diode equivalent circuit comprising a photogenerated current source (I_{ph}), a series resistance (R_s), and a shunt resistance (R_{sh}), as shown in **Figure 1** [9] [10].

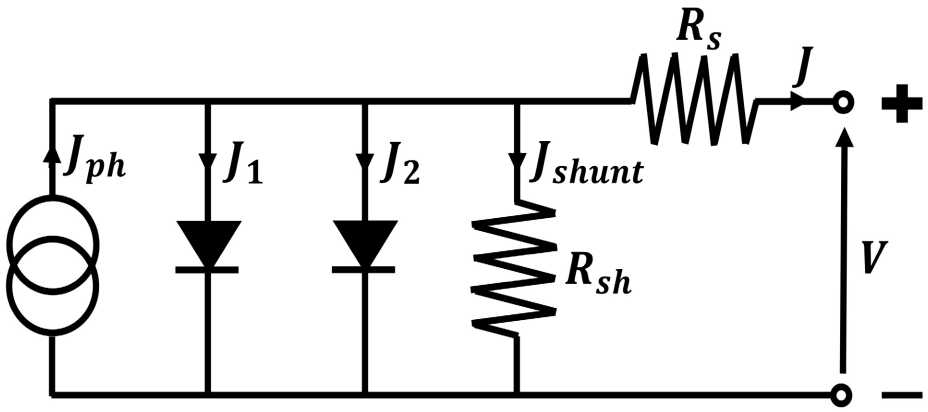

Figure 1. Equivalent electrical circuit of a CIGS thin-film solar cell.

In this framework, R_s aggregates ohmic losses due to the sheet resistance of the transparent conducting oxide (i-ZnO/ZnO:Al), interfacial resistances, the back contact (Mo/CIGS), and the bulk resistivity of the active layers, whereas R_{sh} accounts for leakage currents that partially short the junction (pinholes, percolation along grain boundaries, deep defects, metallic impurities) [9] [11]. The two diodes represent distinct recombination pathways (space-charge region vs. quasi-neutral regions), which enables faithful reproduction of the dark and illuminated *J-V* characteristics and of the impact of R_s and R_{sh} on the fill factor (*FF*) and the power conversion efficiency (PCE) [8]-[10].

2.2. Electrical Parameters

2.2.1. Current Density-Voltage Characteristic $J(V)$

The current density delivered by a CIGS thin-film solar cell under load, within the two-diode model, is written as:

$$J = J_{ph} - J_{01}\left\{\exp\left[\frac{q(V+R_sJ)}{n_1k_BT}\right]-1\right\} - J_{02}\left\{\exp\left[\frac{q(V+R_sJ)}{n_2k_BT}\right]-1\right\}-\frac{V+R_sJ}{R_{sh}} \quad (1)$$

where J_{01} and J_{02} are the saturation current densities (A·cm^{-2}), n_1 and n_2 are the diode ideality factors, R_s and R_{sh} are the (area-normalized) series and shunt resistances (Ω·cm^2), J is the current density (A·cm^{-2}), q the elementary charge (C), k_B the Boltzmann constant (J·K^{-1}), T the temperature (K), V the terminal voltage, and J_{ph} the photogenerated current density (A·cm^{-2}) [11]. The *J-V* characteristic is measured under standard test conditions (STC), typically AM1.5G spectrum, $T = 25^{\circ}\mathrm{C}$, and irradiance $G = 1000\ \mathrm{W}\cdot\mathrm{m}^{-2}$ [12].

2.2.2. Short-Circuit Current Density J_{sc}

The short-circuit current density, measured at $V = 0$, ideally equals the photocurrent ($J_{sc} \approx J_{ph}$). It depends on irradiance and spectrum, optical absorption and reflection, device thickness/quality, and minority-carrier diffusion lengths. A general expression is:

$$J_{sc} = q\int_0^{\lambda_g} I_O(\lambda)\frac{\lambda}{hc}EQE(\lambda)\mathrm{d}\lambda \approx q\int_0^{\lambda_g} I_O(\lambda)\frac{\lambda}{hc}\mathrm{d}\lambda \quad (\text{if } EQE \simeq 1) \tag{2}$$

where $I_O(\lambda)$ is the spectral irradiance (W·cm^{-2}·nm^{-1}), h is Planck's constant (J·s), c is the speed of light in vacuum (m·s^{-1}), λ is the wavelength (m), and λ_g is the cutoff wavelength associated with the absorber's optical bandgap [11].

Here $EQE(\lambda)$ is the external quantum efficiency (electrons collected per incident photon; $0 \le EQE \le 1$), *i.e.*, the fraction of incident photons at wavelength λ that generate carriers collected at the external circuit.

In (2), we assume $EQE(\lambda) \approx 1$ and negligible front-side reflection $R_{front}(\lambda) \approx 0$. This first-order simplification is reasonable for an optically optimized device (e.g., low-reflectance TCO window with an anti-reflective coating and/or surface texturing), for which nearly all above-bandgap photons generate carriers that are actually collected. Formally, writing $EQE(\lambda) = IQE(\lambda)\left[1 - R_{front}(\lambda)\right]A(\lambda)$ we adopt the upper-bound approximation $IQE \to 1$, $R_{front} \to 0$, and $A(\lambda) \to 1$ for $\lambda < \lambda_g$.

Where:

$IQE(\lambda)$: the internal quantum efficiency,

$R_{front}(\lambda)$: the front-side spectral reflectance,

$A(\lambda)$: the spectral absorptance of the device,

λ_g: the bandgap wavelength of the absorber.

2.2.3. Open-Circuit Voltage V_{oc}

At open circuit, $J = 0$. In the single-diode effective approximation one obtains:

$$V_{oc} = \frac{nk_BT}{q}\cdot\ln\left(\frac{J_{SC}}{J_o} + 1\right) \tag{3}$$

where n is the (effective) ideality factor, typically $1 \le n \le 2$ [13].

2.2.4. Fill Factor (*FF*)

The fill factor is defined by

$$FF = \frac{P_m}{J_{sc}V_{oc}} = \frac{J_mV_m}{J_{sc}V_{oc}} \tag{4}$$

with (J_m, V_m) the current density and voltage at the maximum-power point. The fill factor can be written as:

$$FF = FF_{id} \cdot \left(1 - \frac{V_{OC}}{R_{Sh} J_{SC}} - \frac{J_{SC} R_S}{V_{OC}} + \frac{R_S}{R_{Sh}}\right) \tag{5}$$

where FF_{id} is the ideal fill factor of the cell [11] [12].

2.2.5. Power-Conversion Efficiency

The efficiency is the ratio of the maximum electrical power density to the incident optical power density:

$$\eta = \frac{P_m}{P_{in}} = \frac{J_{sc} V_{oc} FF}{P_{in}} \tag{6}$$

where P_{in} is the incident irradiance (e.g., 100 mW·cm^{-2} under STC) [11] [14].

3. Numerical Simulation

3.1. Materials, Structure, and Method

3.1.1. Materials

The thin-film solar cell under study consists of a polyethylene terephthalate (PET) substrate, a molybdenum (Mo) back contact, a Cu(In, Ga)Se_2 (CIGS) absorber, a CdS buffer layer, a ZnO window (transparent conducting oxide, TCO), and two aluminum metal fingers deposited on the TCO to collect the front-side current [3] [4] [15].

3.1.2. Structure

The stack is Al/ZnO/CdS/CIGS/Mo/PET, in a substrate configuration (front-side illumination through the TCO window and Al grid). The structural schematic is shown in **Figure 2** [3] [5] [16].

3.1.3. Method

We investigate, by numerical simulation, the influence of two key absorber parameters, optical bandgap E_g and electron affinity χ on the photovoltaic figures of merit (short-circuit current density J_{sc}, open-circuit voltage V_{oc}, fill factor FF, and efficiency η). Calculations are performed using SILVACO ATLAS, by solving Poisson's equation and the carrier continuity equations coupled with the drift-diffusion transport model [7] [8].

3.1.4. Simulation Parameters

Layer thicknesses follow the reference device specifications from our laboratory when available; the remaining parameters are taken from the literature [3] [7] [8]. A parametric analysis is conducted over the following ranges:

- CIGS bandgap E_g from 1.14 to 1.50 eV;
- Electron affinity χ from 4.0 to 4.8 eV;
- CIGS thickness from 0.1 to 3.0 μm.

Unless stated otherwise, the absorber doping is fixed at 1×10^{16} cm^{-3}, a value retained from our previous simulations.

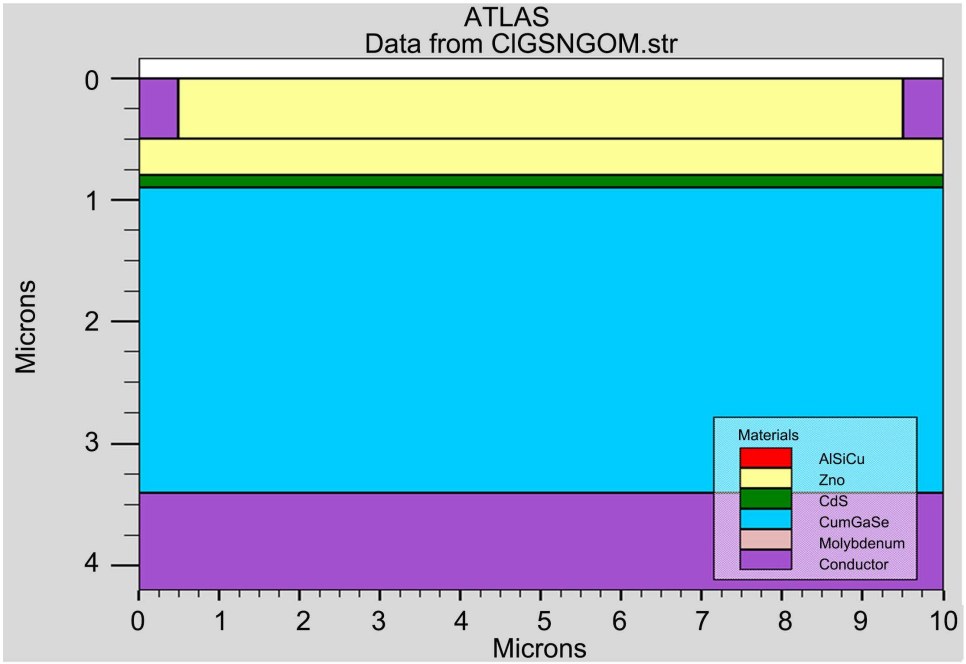

Figure 2. Schematic of the simulated CIGS cell structure (substrate configuration).

Numerical convergence. We verified convergence by refining the mesh (halving Δx and Δy in ZnO/CdS/CIGS and near the electrodes), reducing the voltage sweep step (vstep: 20 mV → 10 mV → 5 mV), and doubling the spectral discretization (120 → 240 wavelengths). Deviations in V_{oc}, J_{sc}, *FF*, and J_0 remained <0.5% (or <0.3 mA·cm^{-2} for J_{sc} and <0.3 percentage point for FF. The time per bias point reported by ATLAS ranges from 0.01 to 0.05 s with the final setup.

Table 1 and Table 2 present the optoelectronic and geometric parameters (Table 1), as well as the defect parameters in the various layers (Table 2).

Table 1. Material properties (input parameters used in the simulations).

Materials	CIGS	CdS	ZnO
Optical bandgap E_{g300} (eV)	1.14 - 1.5	2.4	3.3
Thickness d (μm)	0.1 - 3 μm	0.1	0.8
Electron affinity χ (eV)	4.0 - 4.8	4.5	4.1
Relative dielectric permittivity ε_r	13.6	10	9
Effective electron state density N_{C300} (cm^{-3})	2.2. × 10^{18}	2.2. × 10^{18}	2.2. × 10^{18}
Effective hole state density N_{V300} (cm^{-3})	1.8 × 10^{19}	1.8 × 10^{19}	1.8 × 10^{19}
Electron mobility μ_n (cm^2·V^{-1}·s^{-1})	100	100	100
Hole mobility μ_p (cm^2·V^{-1}·s^{-1})	25	25	25
Electron lifetime τ_n (s)	1 × 10^{-7}	1 × 10^{-7}	1 × 10^{-7}
Hole lifetime τ_p (s)	1 × 10^{-7}	1 × 10^{-7}	1 × 10^{-7}
Acceptor concentration N_A (cm^{-3})	6. × 10^{16}	-	-
Donor concentration N_D (cm^{-3})	-	1. × 10^{18}	1. × 10^{18}

Table 2. Defect properties.

Materials	CIGS	CdS	ZnO
Gaussian defect concentration (cm^{-3})	$N_{DG}=1.\times10^{14}$	$N_{DA}=1.\times10^{15}$	$N_{DA}=1.\times10^{15}$
Gaussian defect concentration (cm^{-3})	0.1	0.1	0.1
Peak energy E_{GA} and E_{GD} (eV)	0.6	1.2	1.65
Electron capture cross section σ_n (cm^2)	$1.\times10^{-17}$	$1.\times10^{-17}$	$1.\times10^{-17}$
Hole capture cross section σ_p (cm^2)	$1.\times10^{-15}$	$1.\times10^{-15}$	$1.\times10^{-15}$

4. Results and Discussion

4.1. Effect of the Absorber Optical Bandgap

The optical bandgap of the CIGS absorber is given by:

$$E_g = 1.04 + 0.64x - 0.15x(1-x) \tag{7}$$

where $x = \mathrm{Ga}/(\mathrm{In}+\mathrm{Ga})$ is the gallium content [7].

This relation shows that the CIGS bandgap is tunable from 1.04 to 1.68 eV. By varying x from 0.2 to 0.8, we obtained bandgap values in the 1.14 - 1.50 eV range. In what follows, we analyze how E_g affects the $J(V)$ characteristic, the short-circuit current density, the open-circuit voltage, the fill factor, and the cell efficiency.

4.1.1. Effect of Absorber Bandgap on the Current-Voltage Characteristic

Figure 3 shows the current-density evolution as a function of voltage for different absorber bandgap values.

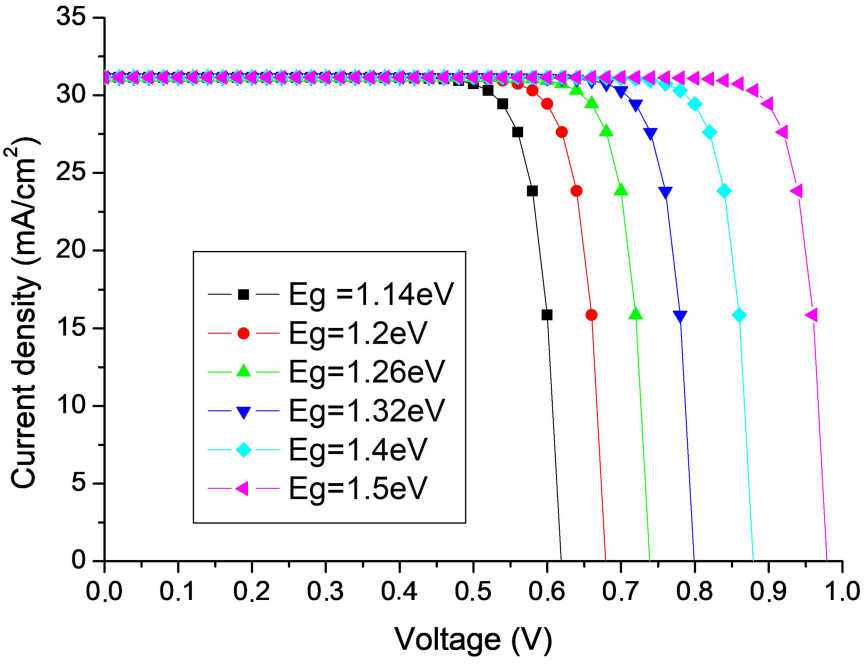

Figure 3. Current-density-voltage characteristics for different absorber bandgaps in CIGS.

Figure 3 shows that all *J-V* curves intersect the current axis at the same point ($J_{sc} = 31.15\ \text{mA}\cdot\text{cm}^{-2}$), while they cross the voltage axis at different values: 0.61 V, 0.67 V, 0.73 V, 0.79 V, 0.87 V, and 0.98 V. In other words, the short-circuit current remains identical, whereas the open-circuit voltage increases with the absorber bandgap E_g. Under the present simulation conditions, the bandgap does not affect J_{sc} but raises V_{oc}, consistent with a reduced effective saturation current. To substantiate these trends, we examine the effect of E_g separately on J_{sc} and V_{oc} [17].

4.1.2. Effect of Absorber Bandgap on the Short-Circuit Current

As outlined above, Figure 4 reports J_{sc} versus E_g for several absorber thicknesses. Over our parameter range, J_{sc} is nearly invariant with E_g, with minor scatter attributable to thickness-dependent optical losses [17].

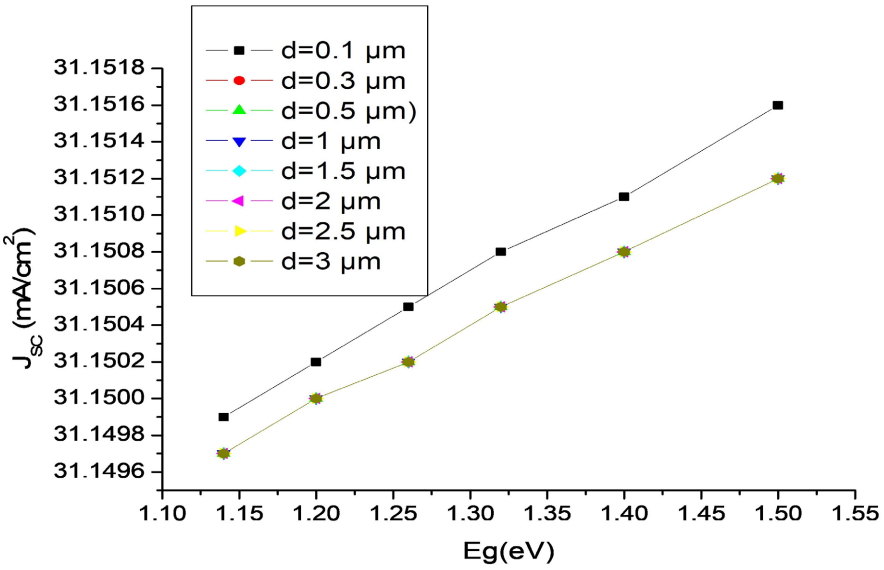

Figure 4. Short-circuit current density versus CIGS absorber bandgap for different thicknesses.

Figure 4 shows that for absorber thicknesses between 0.3 and 3 µm, the short-circuit current density remains essentially unchanged as the bandgap E_g is varied from 1.14 to 1.50 eV. In contrast, for a very thin absorber (0.1 µm), J_{sc} changes appreciably, indicating increased optical losses (residual transmission) in an under-thick layer. Hence, over the explored range, E_g has no significant impact on J_{sc} once the absorber is sufficiently thick, while thickness-dependent optics accounts for the deviation at 0.1 µm. The optimum J_{sc} occurs around 0.3 - 0.5 µm, consistent with the integral form of J_{sc} (Equation (2)) and its dependence through EQE [6].

4.1.3. Effect of Absorber Bandgap on Open-Circuit Voltage

Figure 5 shows the variation of the open-circuit voltage as a function of the optical bandgap of the absorber layer, for different thickness values.

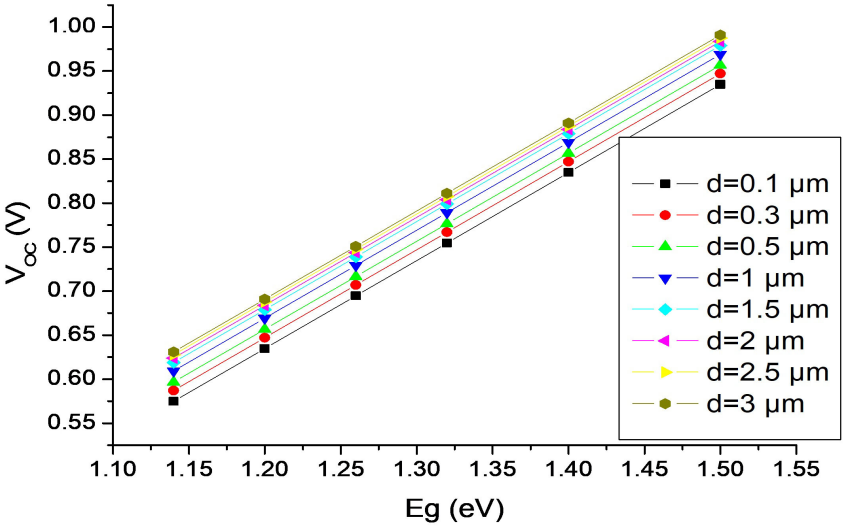

Figure 5. Variation of the open-circuit voltage as a function of the optical bandgap of the CIGS absorber, for different thickness values of the layer.

Figure 5 indicates that the open-circuit voltage V_{oc} increases for all thicknesses from 0.1 to 3 µm as E_g rises from 1.14 to 1.50 eV. This trend is attributed to the decrease in effective saturation current with wider bandgap, which, according to Equation (3), yields a larger V_{oc} [18].

4.1.4. Effect of Absorber Bandgap on the Fill Factor (*FF*)

Figure 6 shows the variation of the fill factor as a function of the optical bandgap of the absorber layer, for different thickness values.

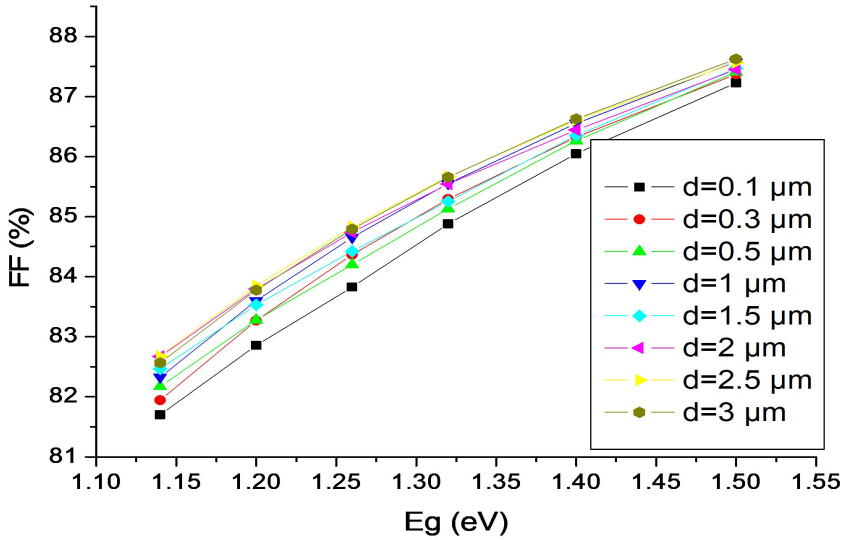

Figure 6. Variation of the fill factor as a function of the optical bandgap of the CIGS absorber, for different absorber thickness values.

From **Figure 6**, the fill factor improves as E_g increases within 1.14 - 1.50 eV for thicknesses of 0.1 - 0.3 µm. The rise is particularly pronounced (81.9435% →

84.3659%) at 0.3 μm when E_g changes from 1.14 to 1.26 eV. This FF enhancement mainly reflects the dependence of FF_{id}, while first-order resistive corrections remain unchanged (Equation (4), Equation (5)).

For $\chi_{\mathrm{CIGS}} = 4.45\,\mathrm{eV}$, the saturation currents simulated under STC are $J_0(n=1) = 1.18\times10^{-14}\,\mathrm{A\cdot cm^{-2}}$ and $J_0(n=2) = 2.16\times10^{-8}\,\mathrm{A\cdot cm^{-2}}$, consistent with the observed trends in V_{oc} and FF.

4.1.5. Effect of Absorber Bandgap on Efficiency

Figure 7 depicts how the optical bandgap of the CIGS absorber influences the solar cell efficiency for different values of layer thickness.

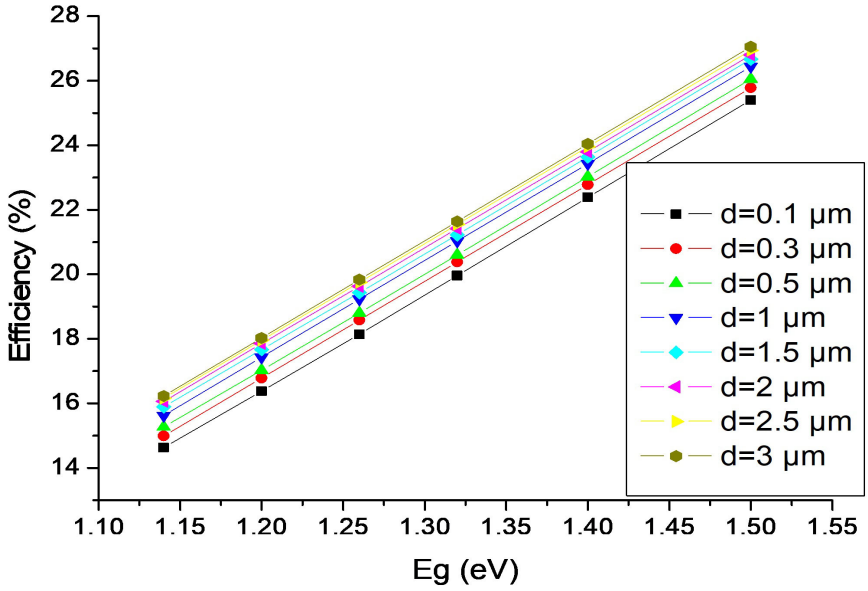

Figure 7. Variation of the conversion efficiency as a function of the optical bandgap of the CIGS absorber, for different absorber thickness values.

Figure 7 shows that the efficiency η increases (from 14.63% to 27.05%) as E_g grows from 1.14 to 1.50 eV for thicknesses between 0.1 and 3 μm. The gain results from stable J_{sc} (except at 0.1 μm) together with increasing V_{oc} and FF. Therefore, a moderate widening of the absorber bandgap can enhance CIGS device performance.

In summary, the bandgap does not significantly affect J_{sc} beyond 0.3 μm, but it raises V_{oc}, FF, and η. Targeting $E_g \approx 1.50$ eV is thus a sound optimization route [19] [20].

Because optical effects (front-side reflection, residual transmission, and surface losses) are not explicitly modeled here, the integral in (2) tends to overestimate J_{sc} and, consequently, the efficiency η. The magnitude of this bias depends on the actual $R_{front}(\lambda)$ and $EQE(\lambda)$ of the device.

4.2. Effect of the Absorber Electron Affinity

The electron affinity of a semiconductor is the energy required to lift an electron

from the conduction band edge to the vacuum level:

$$\chi = E_0 - E_c \tag{8}$$

where E_0 is the vacuum energy and E_c the conduction-band edge.

We now examine how χ affects the $J(V)$ characteristic, short-circuit current, open-circuit voltage, fill factor, and efficiency.

Experimentally, the target electron-affinity range can be reached by tuning the Ga fraction $x = \mathrm{Ga}/(\mathrm{Ga}+\mathrm{In})$ during co-evaporation/three-stage selenization (Ga-grading), since for $\mathrm{Cu}(\mathrm{In}_{1-x}\mathrm{Ga}_x)\mathrm{Se}_2$ the electron affinity follows $\chi(x) \approx 4.61 - 1.162x + 0.034x^2$ eV, and recent work demonstrates such control via engineered Ga profiles [21] [22].

For context between 2023 and 2025, SCAPS-1D modeling studies project CIGS efficiencies above 24%, e.g., 24.43% with a p-Si BSF [23], >31% with an Sb_2S_3 BSF [24], and 24.61% with a $CuAlO_2$ BSF [25]. On the experimental side for single-junction devices, the best cells reported over the same period remain below 24% (~23% - 23.6% under STC), which underscores the value of the optimizations investigated here (increasing E_g, reducing J_0, and engineering the BSF/contacts) to bring real-world performance closer to the simulated potential.

4.2.1. Effect of Electron Affinity on the Current-Voltage Characteristic

Figure 8 reports the current-density as a function of voltage for several values of the absorber χ in CIGS.

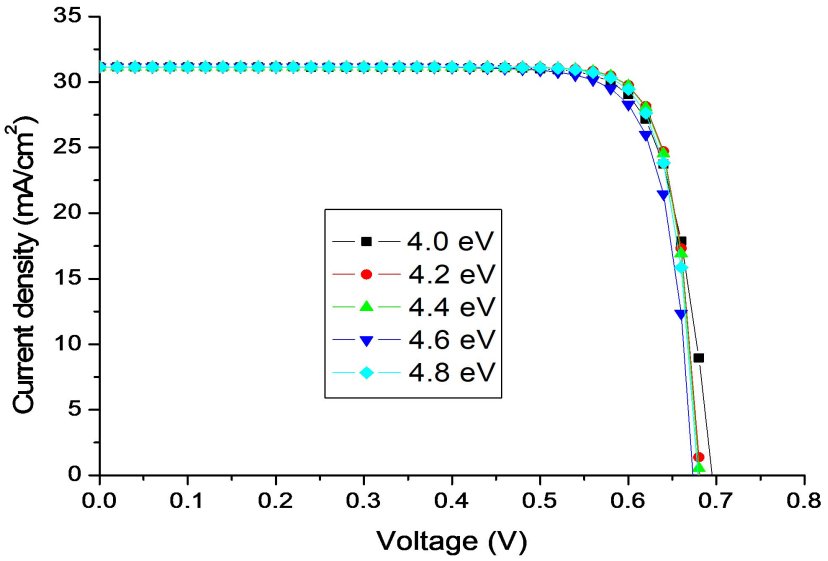

Figure 8. Current-density-voltage characteristics for different electron affinities of the CIGS absorber.

Figure 8 shows that all *J-V* curves intersect the current axis at the same point ($J_{sc} = 31.15$ mA·cm^{-2}) as the electron affinity χ is swept from 4.0 to 4.8 eV. In contrast, the voltage-axis intercept varies: about 0.69 V at $\chi = 4.0$ eV, 0.68 V at $\chi = 4.2$ or 4.4 eV, and 0.67 V at $\chi = 4.6$ or 4.8 eV. Hence, χ does not mate-

rially affect J_{sc} in our range, whereas V_{oc} generally decreases with increasing χ (with a slight leveling at the upper end). To confirm these trends, we analyze J_{sc} and V_{oc} versus χ separately [26].

4.2.2. Effect of Electron Affinity on Short-Circuit Current

Figure 9 illustrates the variation of the short-circuit current density as a function of the electron affinity of the CIGS absorber layer, for different absorber thickness values.

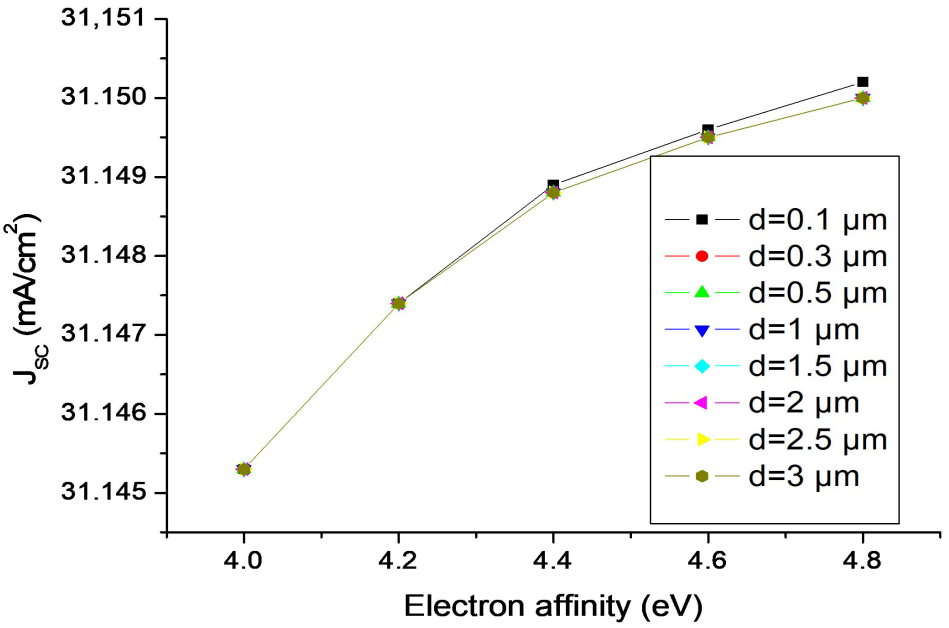

Figure 9. Evolution of the short-circuit current density as a function of the electron affinity of the CIGS absorber, for various thickness values.

Figure 9 shows that J_{sc} remains unchanged for absorber thicknesses between 0.3 and 2 µm as χ varies from 4.0 to 4.8 eV. For a very thin absorber (0.1 µm), J_{sc} is constant from 4.0 to 4.2 eV, then changes as χ increases from 4.2 to 4.8 eV. Thus, the influence of χ on J_{sc} emerges only when the absorber is too thin (<0.3 µm), where band alignment and thickness-dependent optics weigh more heavily on carrier collection [9].

4.2.3. Effect of Electron Affinity on Open-Circuit Voltage

Figure 10 shows the evolution of the open-circuit voltage as a function of the electron affinity of the absorber layer, for various thickness values.

As shown in Figure 10, V_{oc} decreases for all thicknesses (0.1 - 3 µm) as χ rises from 4.0 to 4.6 eV, followed by a slight recovery toward 4.8 eV. This behavior is consistent with an increase in effective saturation current J_0 when the band alignment deteriorates (e.g., a conduction-band cliff), which reduces V_{oc} via Equation (3); when the offset approaches a more favorable regime (e.g., a small spike), interface recombination drops and V_{oc} recovers [10] [27].

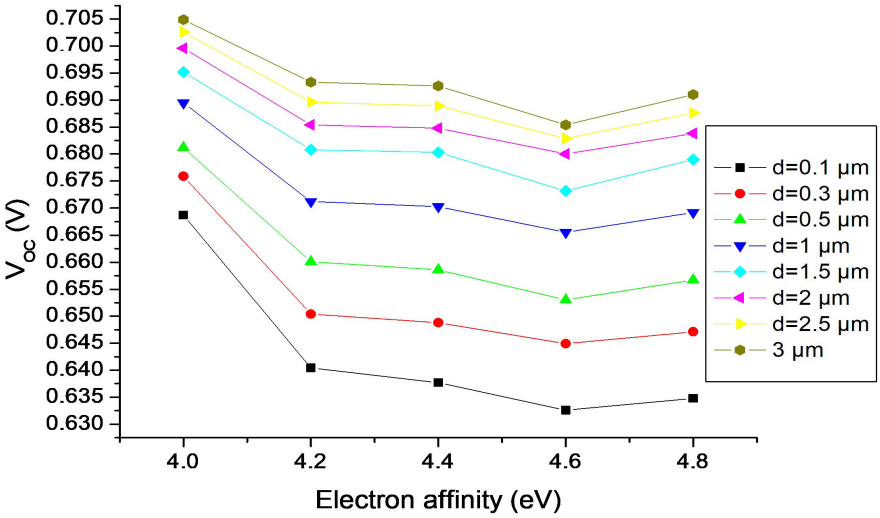

Figure 10. Evolution of the open-circuit voltage as a function of the electron affinity of the CIGS absorber for various thickness values.

4.2.4. Effect of Electron Affinity on the Fill Factor

Figure 11 shows the variation of the fill factor as a function of the electron affinity of the absorber layer, for various thickness values.

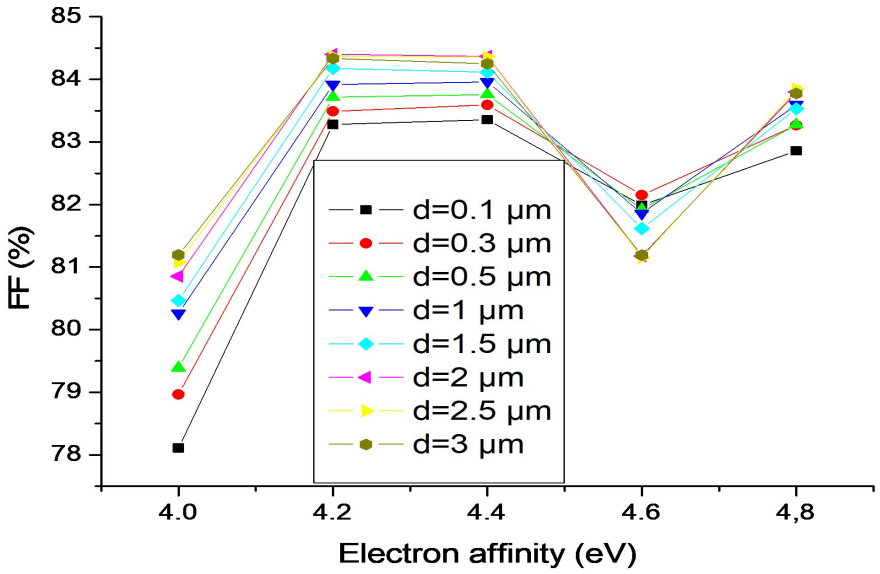

Figure 11. Evolution of the fill factor as a function of the electron affinity of the CIGS absorber for various thickness values.

From **Figure 11**, the fill factor improves for χ 4.0 → 4.2 eV and 4.6 → 4.8 eV, while it degrades within 4.2 → 4.6 eV, across all thicknesses (0.1 - 3 µm). This response reflects the combined evolution of V_{oc} (setting FF_{id}) and resistive losses (first-order in R_s and R_{sh}, Equation (4), Equation (5)). A less favorable offset in the 4.2 - 4.6 eV window enhances interface recombination (apparent rise of J_0), thereby lowering FF; near 4.0 - 4.2 and 4.6 - 4.8 eV, a better alignment

mitigates losses and raises FF.

4.2.5. Effect of Electron Affinity on Efficiency

Figure 12 shows the evolution of the conversion efficiency as a function of the electron affinity of the absorber layer, for various thickness values.

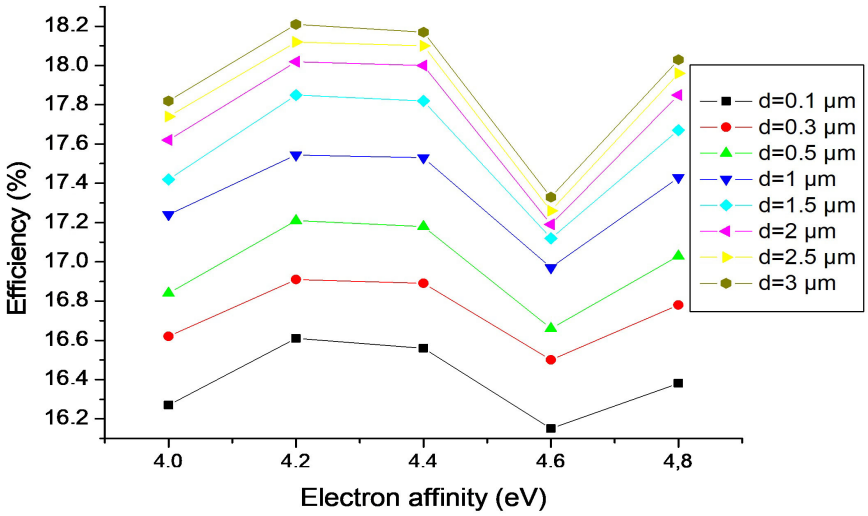

Figure 12. Evolution of the conversion efficiency as a function of the electron affinity of the CIGS absorber for various thickness values.

Figure 12 shows that the efficiency η increases when χ goes from 4.0 to 4.2 eV and from 4.6 to 4.8 eV, but declines between 4.2 and 4.6 eV, for all thicknesses (0.1 - 3 µm). This mirrors the behavior of FF and V_{oc}: the central dip is consistent with an increase of J_0 (recombination/leakage) in the less favorable offset region, while the 4.0 - 4.2 and 4.6 - 4.8 eV windows provide a more favorable alignment that enhances η [10] [27].

Partial conclusion. The electron affinity affects J_{sc} only for ultrathin absorbers (<0.3 µm), yet it systematically impacts V_{oc}, FF, and η. For good performance, $\chi \approx 4.0$ - 4.2 eV and $\chi \approx 4.6$ - 4.8 eV appear favorable [28].

5. Conclusions

This study first reviewed the theoretical background and the two-diode equivalent circuit for CIGS cells, together with the governing equations for their electrical parameters. It then detailed the materials, the device structure, and the TCAD methodology used, SILVACO-ATLAS with drift-diffusion transport coupled to Poisson and carrier-continuity equations [7] [8]. Finally, we quantified the impact of the absorber's optical bandgap E_g and electron affinity χ on the figures of merit.

The main findings are as follows:

1) J_{sc} is essentially independent of E_g over 1.14 - 1.50 eV once the absorber is sufficiently thick (≥0.3 µm); a deviation appears at 0.1 µm (enhanced optical losses), while V_{oc}, FF, and η increase with E_g.

2) A maximum efficiency of about 27.05% is achieved for $E_g \approx 1.50$ eV with $d_{\mathrm{CIGS}} = 3\,\mu\mathrm{m}$, where the rise of V_{oc} and FF compensates the near-invariance of J_{sc}.

3) The electron affinity χ affects J_{sc} only for ultrathin absorbers (<0.3 μm); however, it systematically impacts V_{oc}, FF, and η, with favorable windows around $\chi \approx 4.0$ - 4.2 eV and $\chi \approx 4.6$ - 4.8 eV across 0.1 - 3 μm.

These trends support the view that joint engineering of E_g (e.g., via Ga content) and χ (band alignment at the CdS/CIGS and TCO interfaces) is a robust lever for optimizing CIGS thin-film solar cells [6] [19] [20] [27] and [28]. In the longer term, a broader comparison with other chalcogenide absorbers (e.g., Sb_2Se_3) could refine the performance-sustainability trade-offs highlighted here [29].

Conflicts of Interest

The authors declare no conflicts of interest regarding the publication of this paper.

References

[1] Nyarko, F.K.A., Takyi, G. and Amalu, E.H. (2020) Robust Crystalline Silicon Photovoltaic Module (c-Si PVM) for the Tropical Climate: Future Facing the Technology. *Scientific African*, **8**, e00359. https://doi.org/10.1016/j.sciaf.2020.e00359

[2] Zhao, C., Yu, S., Tang, W., Yuan, X., Zhou, H., Qi, T., *et al.* (2023) Advances in CIGS Thin Film Solar Cells with Emphasis on the Alkali Element Post-Deposition Treatment. *Materials Reports*: *Energy*, **3**, Article 100214. https://doi.org/10.1016/j.matre.2023.100214

[3] Faraj, M.G., Ibrahim, K. and Salhin, A. (2012) Fabrication and Characterization of Thin-Film Cu (in, Ga) Se_2 Solar Cells on a PET Plastic Substrate Using Screen Printing. *Materials Science in Semiconductor Processing*, **15**, 165-173. https://doi.org/10.1016/j.mssp.2011.10.006

[4] Kyriakides, E., Nicolaou, C., Ioannou, P.S., Papagiorgis, P., Itskos, G. and Giapintzakis, J. (2024) Single-Stage Fabrication of Buffer and Window Layers of CIGS Thin-Film Solar Cells Using Pulsed Laser Deposition. *Solar Energy*, **283**, Article 112993. https://doi.org/10.1016/j.solener.2024.112993

[5] Amare, A.M., Hwang, I., Jeong, I., Park, J.H., An, J.G., Song, S., *et al.* (2025) High-efficiency Cadmium-Free Cu (In, Ga) Se2 Flexible Thin-Film Solar Cells on Ultra-Thin Glass as an Emerging Substrate. *Journal of Alloys and Compounds*, **1024**, Article 180187. https://doi.org/10.1016/j.jallcom.2025.180187

[6] Sharma, I., Pawar, P.S., Kumar Yadav, R., Nandi, R. and Heo, J. (2022) Review on Bandgap Engineering in Metal-Chalcogenide Absorber Layer via Grading: A Trend in Thin-Film Solar Cells. *Solar Energy*, **246**, 152-180. https://doi.org/10.1016/j.solener.2022.09.046

[7] Bouanani, B., Joti, A., Bachir Bouiadjra, F.S. and Kadid, A. (2020) Band Gap and Thickness Optimization for Improvement of CIGS/CIGS Tandem Solar Cells Using Silvaco Software. *Optik*, **204**, Article 164217. https://doi.org/10.1016/j.ijleo.2020.164217

[8] Ghorbani, T., Zahedifar, M., Moradi, M. and Ghanbari, E. (2020) Influence of Affinity, Band Gap and Ambient Temperature on the Efficiency of CIGS Solar Cells. *Optik*, **223**, Article 165541. https://doi.org/10.1016/j.ijleo.2020.165541

[9] Uddin, M.S., Hosen, R., Sikder, S., Mamur, H. and Bhuiyan, M.R.A. (2024) Photovol-

taic Performance Enhancement of Al/ZnO: Al/i-ZnO/CdS /CIGS/Pt Solar Cell Using SCAPS-1D Software. *Next Energy*, **2**, Article 100080. https://doi.org/10.1016/j.nxener.2023.100080

[10] Mohottige, R.N. and Kalawila Vithanage, S.P. (2021) Numerical Simulation of a New Device Architecture for Cigs-Based Thin-Film Solar Cells Using 1D-SCAPS Simulator. *Journal of Photochemistry and Photobiology A*: *Chemistry*, **407**, Article 113079. https://doi.org/10.1016/j.jphotochem.2020.113079

[11] Mouhoub, A. (2020) Optimization of Thin-Film CIGS Absorbers for Bifacial Solar Cells. Ph.D. Thesis, Institutional Repository of Ferhat ABBAS University. http://dspace.univ-setif.dz:8888/jspui/handle/123456789/3582

[12] Ziar, H. (2024) Protocol to Simulate Crystalline Si-Based Single and Multi-Junction Solar Cells under Standard Test and Real-World Conditions via MATLAB Scripts. *STAR Protocols*, **5**, Article 103464. https://doi.org/10.1016/j.xpro.2024.103464

[13] Pepa, P.E., Afungchui, D., Holtomo, O. and Ebobenow, J. (2025) Parameters Critically Affecting the Open Circuit Voltage of an Organic Solar Cell. *Heliyon*, **11**, e42684. https://doi.org/10.1016/j.heliyon.2025.e42684

[14] Malik, M., Masud, M.I., Kashif, M., Tariq, M.U.N., Alqarni, M. and Shafqat, S.S. (2025) Optimizing Power Conversion Efficiency in $(Fa)_2BiCuI_6$ Double Perovskite Solar Cells: Advanced Strategies for Performance Enhancement. *Results in Engineering*, **27**, Article 106124. https://doi.org/10.1016/j.rineng.2025.106124

[15] Kakade, A., Chavan, K.B., Chaure, S. and Chaure, N.B. (2025) The Role of Window Layers on the Simulated Performance of CIGS Solar Cell Characteristics Using Scaps-1d. *Next Research*, **2**, Article 100334. https://doi.org/10.1016/j.nexres.2025.100334

[16] Kumbhar, K.R., Redekar, R.S., Raule, A.B., Shirage, P.M., Jang, J.H. and Tarwal, N.L. (2025) Predictive Modeling and Optimization of CIGS Thin Film Solar Cells: A Machine Learning Approach. *Solar Energy*, **294**, Article 113509. https://doi.org/10.1016/j.solener.2025.113509

[17] Hajji, M., Akkari, A., Charrada, G., Garcia-Loureiro, A. and Kamoun, N. (2025) Improving CIGS Solar Cell Efficiency through Single, Double, and Triple Junction Absorber Layer Design Innovations. *Ceramics International*, **51**, 25426-25436. https://doi.org/10.1016/j.ceramint.2025.03.226

[18] Houmomou, A.M., Tchangnwa Nya, F., Kenfack, G.M.D., Laref, A. and Mohamadou, A. (2024) High-Performance CIGS Solar Cells Using a Double Active Layers Approach—SCAPS 1D Optoelectronic Modeling Approach. *Inorganic Chemistry Communications*, **170**, Article 113426. https://doi.org/10.1016/j.inoche.2024.113426

[19] Elmelouky, A., Zaim, S., Mosonik, B.C., Kibet, J.K. and ElMoznine, R. (2025) In-depth Study of CIGS (Copper, Indium, Gallium, and Selenium) Layer Properties with the Impact of Silicon Layer for Enhancement of Solar Cell Performance. *Materials Science and Engineering*: *B*, **318**, Article 118307. https://doi.org/10.1016/j.mseb.2025.118307

[20] Benahmed, A., Aissat, A., Ayachi, B., Sfina, N., Saidi, F. and Vilcot, J.P. (2024) Efficiency Improvement of Thin Film Cuin1-Xgaxse2 Structure for Solar Cells Applications. *Micro and Nanostructures*, **188**, Article 207801. https://doi.org/10.1016/j.micrna.2024.207801

[21] Zhang, J., Ma, Z., Zhang, Y., Liu, X., Li, R., Lin, Q., *et al.* (2024) Highly Efficient Narrow Bandgap Cu (In, Ga) Se2 Solar Cells with Enhanced Open Circuit Voltage for Tandem Application. *Nature Communications*, **15**, Article No. 10365. https://doi.org/10.1038/s41467-024-54818-6

[22] Asaduzzaman, M., Hasan, M. and Bahar, A.N. (2016) An Investigation into the Effects of Band Gap and Doping Concentration on Cu (In, Ga) Se2 Solar Cell Efficiency. *SpringerPlus*, **5**, Article No. 578. https://doi.org/10.1186/s40064-016-2256-8

[23] Chadel, M., Chadel, A., Benyoucef, B. and Aillerie, M. (2023) Enhancement in Efficiency of CIGS Solar Cell by Using a P-Si BSF Layer. *Energies*, **16**, Article 2956. https://doi.org/10.3390/en16072956

[24] Rahman, M.F., Chowdhury, M., Marasamy, L., Mohammed, M.K.A., Haque, M.D., Al Ahmed, S.R., *et al.* (2024) Improving the Efficiency of a CIGS Solar Cell to above 31% with Sb_2S_3 as a New BSF: A Numerical Simulation Approach by SCAPS-1D. *RSC Advances*, **14**, 1924-1938. https://doi.org/10.1039/d3ra07893k

[25] Kumar, A. and Giripunje, S.M. (2025) A Comparative Numerical Simulation Study of CIGS Solar Cells with Distinct Back Surface Field Layers for Enhanced Performance. *Journal of Physics and Chemistry of Solids*, **197**, Article 112436. https://doi.org/10.1016/j.jpcs.2024.112436

[26] Sikder, S., Hasan, M.K., Mamur, H. and Bhuiyan, M.R.A. (2025) Optimizing Layer Configuration and Material Selection to Enhance CIGS Solar Cell Performance through Computational Simulation. *Hybrid Advances*, **10**, Article 100460. https://doi.org/10.1016/j.hybadv.2025.100460

[27] Kumar, A., Giripunje, S.M., Patel, A.K. and Gohri, S. (2024) Designing and Simulating of New Highly Efficient Ultra-Thin CIGS Solar Cell Device Structure: Plan to Minimize Cost per Watt Price. *Journal of Physics and Chemistry of Solids*, **193**, Article 112194. https://doi.org/10.1016/j.jpcs.2024.112194

[28] El I Boukortt, N. and Loureiro, A.G. (2025) Optimizing World-Record Thin-Film ACIGS Solar Cells with Innovative 'Hockey Stick'-Shaped GGI Profile for Tandem Solar Technology. *Micro and Nanostructures*, **206**, Article 208220. https://doi.org/10.1016/j.micrna.2025.208220

[29] Ezihe, J.A., Abdulwahab, M., Ezema, F.I. and Echendu, O.K. (2025) Essential Properties, Growth Methods, Environmental Impacts, and Solar Cell Application of Antimony Triselenide Thin Films: A Review. *Hybrid Advances*, **10**, Article 100505. https://doi.org/10.1016/j.hybadv.2025.100505

Abbreviations

AM1.5G: Standard solar spectrum (Air Mass 1.5 Global)
CdS: Cadmium sulfide (buffer layer, n-type)
CIGS: Cu(In, Ga)Se_2, chalcopyrite absorber (p-type)
EQE: External Quantum Efficiency
FF: Fill Factor
IQE: Internal Quantum Efficiency
J-V: Current-density-voltage characteristic
PET: Polyethylene terephthalate (substrate)
PCE: Power-conversion efficiency
PLD: Pulsed Laser Deposition
STC: Standard Test Conditions (AM1.5G, 25˚C, 1000 $W \cdot m^{-2}$)
TCAD: Technology Computer-Aided Design (device simulation)
TCO: Transparent conducting oxide
ZnO: Zinc oxide (window layer/TCO)
Mo: Molybdenum (back contact)
Al: Aluminum (front grid/contact)